Corrosion Science 110 (2016) 35–45

Contents lists available at ScienceDirect

Corrosion Science

journal homepage: www.elsevier.com/locate/corsci

A direct measurement of wall shear stress in multiphase flow—Is it an important parameter in CO_2 corrosion of carbon steel pipelines?

Wei Li*, B.F.M. Pots, Bruce Brown, Kok Eng Kee, Srdjan Nesic

Institute for Corrosion and Multiphase Technology, Department of Chemical and Biomolecular Engineering, Ohio University, Athens, OH 45701, United States

ARTICLE INFO

Article history:
Received 27 January 2016
Received in revised form 23 March 2016
Accepted 10 April 2016
Available online 11 April 2016

Keywords:
Wall shear stress
Acid corrosion
Carbon steel
Gas-liquid slug flow
Flow loop

ABSTRACT

Wall shear stress produced by turbulent multiphase flow is considered an important parameter in CO_2 corrosion as it has been claimed to be responsible for the removal of protective corrosion product layers and corrosion inhibitor films. In this study, a floating element wall probe was used to directly measure wall shear stress in multiphase flow; the highest measured values were of the order of 100 Pa. Findings suggest that the wall shear stress alone, produced in multiphase flow patterns covered in the present study, is insufficient to mechanically damage the protective corrosion product layers or corrosion inhibitor films.

1. Introduction

Carbon steel pipelines and piping used in transportation of hydrocarbon products are prone to internal corrosion when exposed to an aqueous CO_2 environment [1]. The general mechanisms of CO_2 corrosion have been extensively researched and are well understood [1,2].

Mitigation of CO_2 corrosion can be achieved by the use of organic corrosion inhibitors which form a thin film (order of nm) on the steel surface or by reliance on formation of protective corrosion product layers, such as iron carbonate (thickness of the order of 10 μm). Regardless of the mechanisms of their adhesion to the metal surface, both form a protective barrier [3–7]. The reduction in corrosion rate depends upon the structure and integrity of these films or layers. Any partial damage or removal of these films or layers may lead to initiation and propagation of localized corrosion through the development of galvanic cells [4,8,9].

The effects of flow on the integrity of protective inhibitor films and corrosion product layers have been attributed to mass transfer, mechanical forces, and other factors such as the presence of solid particles [10]. Flow enhances the mass transport of corrosive species (e.g., H^+) from bulk solution to the steel surface and accelerates the corrosion of the underlying steel [11]; flow also facilitates the mass transport of the corrosion product (Fe^{2+}) away from the steel surface and hinders the formation of protective iron carbonate layers [10].

The effect of mechanical forces exerted by single-phase or multiphase flow on these films or layers is not well understood. On one hand, experience from field and some laboratory experiments indicates that protective films and corrosion product layers can fail at a high flow velocity [12–15]; in those cases high wall shear stress (WSS) has often been suggested as the main culprit [13,16–18]. On the other hand, some detailed laboratory experiments, that isolated pure mechanical effect of flow, found that high WSS in turbulent flow conditions did not affect inhibitor films [19] or corrosion product layers [20]. For example, Gulbrandsen and Grana [19] used a jet impingement setup and found that the CO_2 corrosion inhibitor performance was independent of flow velocity up to 20 m/s with a calculated WSS up to 1400 Pa.

The presence of solid particles in the flow stream can undoubtedly affect corrosion inhibition. At low flow rates settling of particles may lead to under-deposit corrosion [9,21], while at high flow rates the particle-wall impacts may cause damage to inhibitor films and corrosion product layers, often termed erosion-corrosion [22,23].

To answer the question as to whether flow could mechanically damage the protective inhibitor films and corrosion product layers, in the absence of solid particles, the mechanical integrity and adhesion strength of these films/layers to the steel surface were characterized in controlled laboratory experiments. For example, the adhesion strength of the $FeCO_3$ layer to a steel substrate was measured by tensile testing [15,20]. In those experiments, an exter-

* Corresponding author.
E-mail address: wl234208@ohio.edu (W. Li).

http://dx.doi.org/10.1016/j.corsci.2016.04.008
0010-938X/

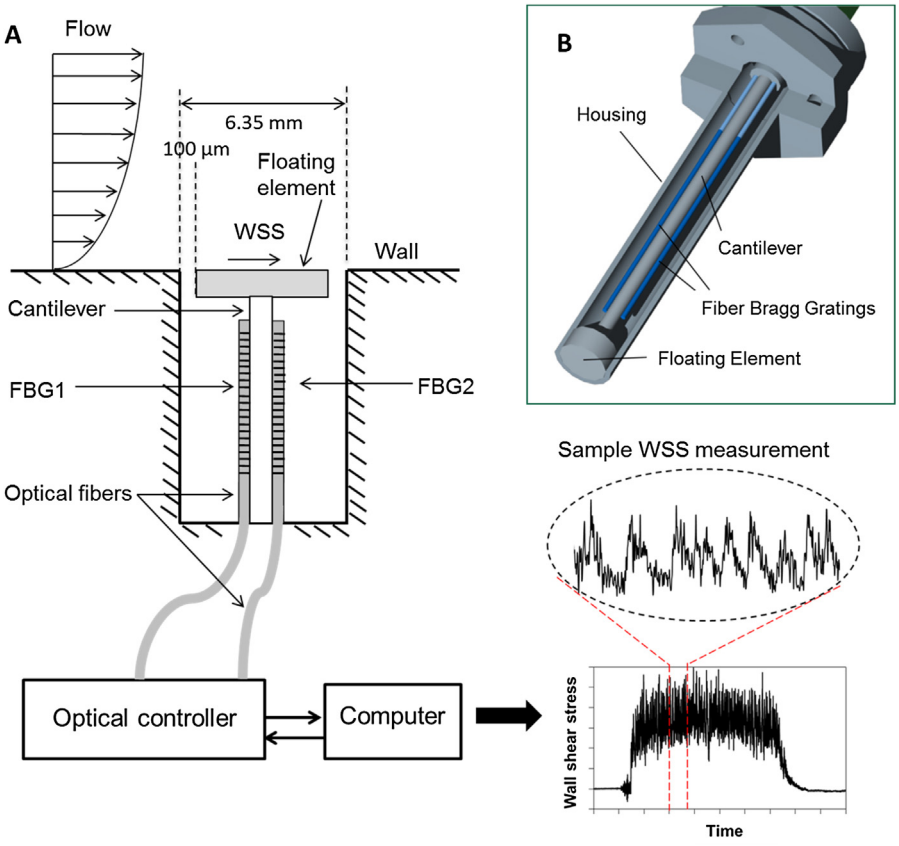

Fig. 1. (A) Schematic of a floating element WSS measurement system showing a sample measurement; (B) schematic diagram of WSS probe body (by Lenterra with permission).

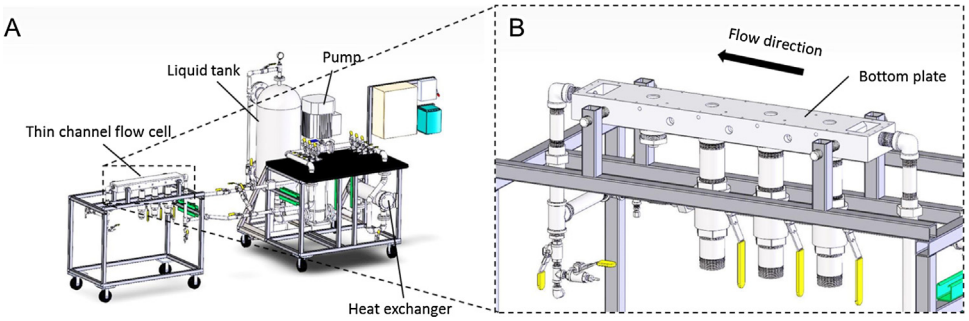

Fig. 2. Visual representations of: (A) thin channel flow cell assembly and (B) zoomed-in view of the bottom plate of the flow cell (top lid not shown).

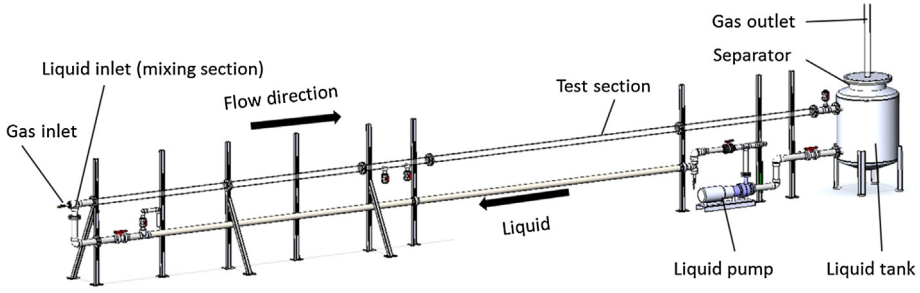

Fig. 3. Representation of 10.2 cm ID pipe flow loop.

nal stud was glued to a $FeCO_3$ layer pre-formed on the steel surface by using a strong adhesive and then separated. The required separation force was measured, and the adhesion strength of the $FeCO_3$ layers to the steel surface was calculated to be of the order of 1–10 MPa. In another study, Xiong et al. [24] used atomic force microscopy (AFM) to mechanically remove an inhibitor film from a steel surface. The adsorbed inhibitor film was "scratched" by the lateral movements of the AFM tip that was in contact with the

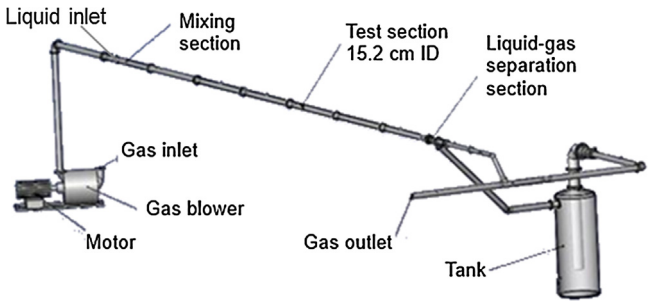

Fig. 4. Representation of 15.2 cm ID once-through pipe system.

steel surface. The required lateral forces to remove the inhibitor molecules from the steel surface were calculated to be of the order of 50–100 MPa. Since these stress values are several orders of magnitude larger than the typical WSS values measured or calculated for multiphase pipe flow [8,10,25], it seems to be impossible that multiphase flow is able to mechanically remove a protective inhibitor film or a corrosion product layer. Before we jump to that conclusion, it is worth noting that a closer inspection of the literature indicates that there are no direct measurements of WSS in multiphase pipe flow, making the above-mentioned reasoning less convincing.

Accurately measuring WSS in multiphase flow is challenging. Very few studies related to WSS in multiphase flow have been conducted in the past [26–28]. There, the WSS was typically obtained from indirect methods, such as: by using an electrochemical mass-transfer sensor or a hot-film heat-transfer sensor, which rely on a correlation between the measured property (mass or heat transfer rate) to the WSS [29,30]. These correlations are justified by using the Reynolds analogy, which is strictly valid only in fully developed single-phase flow with no pressure gradients. Therefore, they have a limited range of validity and their extension to complex multiphase flow conditions is not easily justified.

In the present study, a floating element probe flush mounted on the pipe wall was used to directly measure the WSS in multiphase flow. The floating element is connected to a cantilever with two optical fiber strain gauges attached. The top face of the floating element flush mounted on the internal pipe wall is laterally displaced when there is fluid shearing over its surface. Any movement of the floating element causes bending of the cantilever, which changes the optical reflection spectra obtained from the attached strain gauges. The optical spectra are then processed followed by straightforward mechanical calculations that can indicate the WSS value. In the present work, the direct WSS measurements were complemented by high speed camera video recordings of the flow field.

2. Experimental

2.1. Measurement of WSS

A floating element WSS probe manufactured by Lenterra, Inc.[1] was employed in this study [31]. The schematic of the floating element WSS measurement system is shown in Fig. 1, which comprises a probe, a controller and a computer. The probe consists of a floating element with a supporting cantilever, with two optical strain gauges attached, and a probe enclosure. The circular-shaped floating element is set in a 6.35 mm internal diameter (ID) cylindrical sensor enclosure with a fine external thread pitch of 0.32 mm to ensure a flush alignment with the pipe wall. The nominal gap between the edges of the floating element and the inner wall of the sensor enclosure is 100 μm, which allows for the movement of the floating element. Two optical strain gauges, with fiber Bragg gratings (FBG), are attached to the cantilever. The FBGs are connected to the controller through optical fibers. The computer processes and stores the data. The floating element probe is made from stainless steel and glass fibers, and is therefore robust enabling it to work under fluid immersion conditions.

In principle, direct measurements of WSS rely on accurately measuring the lateral displacement of the floating element. For this probe, the displacement of the floating element due to WSS is translated into the changes of optical signals transmitted by the FBG attached to the cantilever. During a measurement, the optical controller generates a monochromatic light beam from a laser diode. This light is directed to the FBG and the reflected light intensity is measured by a photodiode. The FBG only reflects light at its resonant wavelength and transmits all other wavelengths, which acts as an optical filter. While tuning the input laser wavelength, the reflection spectra (reflected light intensity versus laser wavelength) are recorded, from which the resonant wavelength is determined. The resonant wavelength shifts when the FBG is strained. Therefore, the WSS causing the displacement of the floating element and the deflection of the cantilever are represented by the resonant wavelength shift of the FBG. Temperature change also causes a shift of the resonant wavelength of the FBGs. Using two FBGs at opposite sides of the cantilever compensates for temperature sensitivity. When the cantilever is deflected by the flow, FBG1 is stretched and FBG2 is compressed (Fig. 1). By subtracting their resonant wavelengths, the difference is independent of the temperature [31]. The difference between the resonant wavelengths of the two FBGs due to deflection of the cantilever provides the value of the exerted WSS on the floating element through the equation:

$$\tau = k\Delta\lambda \tag{1}$$

where τ is the wall shear stress, k is a calibration coefficient, and $\Delta\lambda$ is the difference between the resonant wavelengths of the two FBGs. The calibration coefficient is determined by applying a series of known shear forces to the floating element and measuring the corresponding values of $\Delta\lambda$. The WSS probe comes calibrated by the supplier.

In this study, two floating element WSS probes were used, one with a measurement range up to 100 Pa and the other with a measurement range up to 1000 Pa. Their nominal mechanical resonant frequencies are 105 Hz and 235 Hz, respectively. The typical data acquisition rate of the controller was set to 10k samples/s due to the limitations of the system hardware. The WSS data recording rate in the computer was set at either 100 Hz or 1000 Hz by averaging either 100 or 10 samples for each data point. The higher data recording rate of 1000 Hz provided finer temporal resolution, but also required more memory from the computer which limited the total recording time. For data recorded at the 1000 Hz, a low-pass filter was applied to the raw data to remove the noise from the probe mechanical resonance. In the flow patterns studied here, no significant difference was observed when comparing data recorded at 100 Hz and 1000 Hz. Therefore all the results reported below are based on data collected at 100 Hz, which allowed longer recording times.

2.2. Visualization of the flow field

For two-phase flow patterns, a Phantom V12.0[1] high speed video camera was employed for recording of the flow that was also synchronized with the WSS measurements. This allows for the observed and recorded flow events, such as a passage of slug, to be correlated with WSS data. The typical video recording rate was 5000 frames per second (fps). A powerful light source (two 500 W

[1] Trade Name.

Table 1
Test matrix for single-phase flow measurements.

Parameter	Channel Flow	Pipe Flow
Fluid	Deionized water	Deionized water
Flow cross section	rectangular 3 mm x 100 mm	circular 102 mm diameter
Flow velocity	2 m/s–17 m/s	1 m/s–2.9 m/s
Pipe material	Stainless steel	PVC pipe
Temperature/pressure	25 °C/1 atm	25 °C/1 atm

Table 2
Test matrix for horizontal gas-liquid two-phase flow.

Parameter	10.2 cm ID flow loop	15.2 cm ID once-through
Liquid	Water	Water
Gas	CO_2	Air
Superficial liquid velocity range	0.1 m/s–2.9 m/s	0.017 m/s–0.17 m/s
Superficial gas velocity range	0.2 m/s–5 m/s	42 m/s
Pipe Material	PVC pipe	PVC pipe
Temperature/pressure	25 °C/1 atm	25 °C/1 atm
Studied flow patterns	Stratified flow/slug flow	Annular-mist flow

lamps) was placed behind the pipe test section with a paper light diffuser to provide adequate and uniform illumination.

2.3. Equipment

WSS measurements were performed in both single-phase and multiphase flow. Baseline tests in single-phase flow were done to check the performance of the WSS probe and lay the groundwork for application in more complicated flows such as two-phase flow where accurate WSS predictions were expected to be more difficult.

Single-phase flow experiments were performed in two types of flow geometries: bounded channel flow and full pipe liquid flow. For channel flow, a thin channel flow cell (TCFC) system was used—a visual representation is shown in Fig. 2. The flow cell is 600 mm long with a rectangular cross section of 3 mm × 100 mm. Four ports located at the bottom plate of the flow cell allow installation of flush-mounted plug-in probes such as differential pressure transducers and the WSS probe. All wetted parts of the flow loop are made of stainless steel.

For single-phase pipe flow, a 1100 L in volume, 10.2 cm ID, 15 m long horizontal flow loop system was used (Fig. 3). The test section is located about 11 m (109 pipe diameters) downstream of the inlet zone, which was deemed sufficiently long for the flow to fully develop. This flow loop was used for both single-phase and gas-liquid two-phase horizontal flow tests. The liquid velocity and the gas velocity were measured by a paddlewheel flow meter and a hot wire anemometer, respectively. Both meters were calibrated before the experiments. The test matrix for the single-phase flow experiments is shown in Table 1.

Additional experiments in gas-liquid two-phase horizontal flow were performed in a 15.2 cm ID once-through flow system, as shown in Fig. 4. This system is 37 m long. The test section is approximately 27.4 m (180 pipe diameters) downstream of the gas-liquid inlet mixing section. For both the 10.2 cm and 15.2 cm systems, transparent polyvinyl chloride (PVC) pipe sections are used for flow visualization. The 10.2 cm flow loop has a broader superficial liquid velocity (V_{sl}) range (up to 2.9 m/s) compared to the 15.2 cm system (up to 0.2 m/s). On the other hand, the 15.2 cm system has a ten times larger superficial gas velocity (V_{sg}) range (up to 60 m/s). With these two systems, a wide range of horizontal two-phase flow patterns was investigated. Stratified and slug flow were studied in the 10.2 cm flow loop, while annular-mist flow was studied in the 15.2 cm flow system. The test matrix for two-phase flow is given in Table 2.

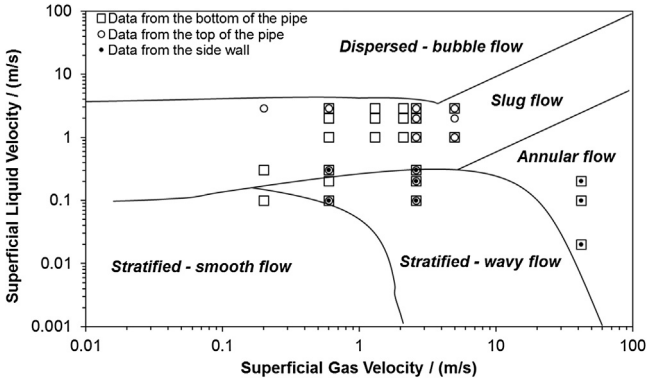

Fig. 5. Tested flow conditions for WSS measurements in a horizontal two-phase flow pattern map for 1 bar, 25 °C, CO_2-water, and 10.2 cm pipe loop.

Since the phases are not homogeneously distributed over the pipe cross section for these two-phase flow patterns, it was necessary to measure the WSS circumferentially around the pipe. Consequently, WSS measurements were conducted at three locations on the pipe wall (bottom, top and side). A repeatable procedure was used for measuring WSS at each of these locations. A full measurement sequence consists of several steps: (a) the WSS probe started recording data at 0 s with no flow; (b) the gas was introduced into the flow loop and reached the required superficial velocity gradually; (c) the liquid was introduced into the flow loop and reached the specified superficial velocity; (d) the desired two-phase flow pattern became fully developed; (e) the liquid supply was shut off; (f) the gas supply was shut off; and (g) the WSS was recorded for another 10 s in order to confirm that there was no offset in the measurement from beginning to end. Although the specific times may vary from test to test, the measurement procedure was the same. WSS measurements were taken with at least one repeat for each flow condition.

The summary of all two-phase flow conditions for which data were collected, is shown in the context of a two-phase flow pattern map generated by an in-house gas-liquid flow model (Fig. 5) [32]. The flow transition lines between stratified-wavy and annular-mist flow for the 10.2 cm and 15.2 cm ID lines, carrying CO_2 and air respectively, are very similar; therefore the annular-mist flow data obtained from the 15.2 cm line was plotted alongside the data collected in the 10.2 cm line in the same flow pattern map.

3. Results

3.1. Wall shear stress measurements in single-phase flow

Correlations for calculating mean WSS in single-phase flow are well-established. The relationship between time-averaged WSS (τ) and mean flow velocity for single-phase flow can be expressed as:

$$\tau = \frac{1}{2}\rho C_f V^2 \tag{2}$$

where ρ is the fluid density (kg/m^3), C_f is the Fanning friction factor, and V is the mean flow velocity (m/s). The Fanning friction factor is a function of the Reynolds number (Re) and surface roughness.

For channel flow, the Patel correlation for a smooth surface can be used to calculate the friction factor [33]:

$$C_f = 0.0376 Re^{-1/6} \tag{3}$$

using the height of channel (h), as the characteristic length to calculate the Reynolds number as discussed before by Patel et al. [33].

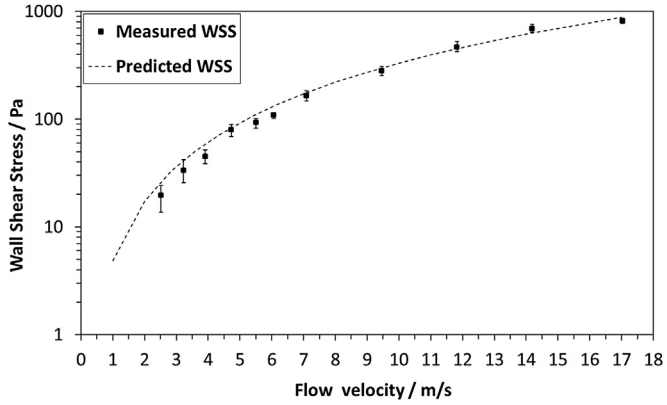

Fig. 6. Comparison of measured WSS values with Patel calculations for channel flow (h = 3 mm).

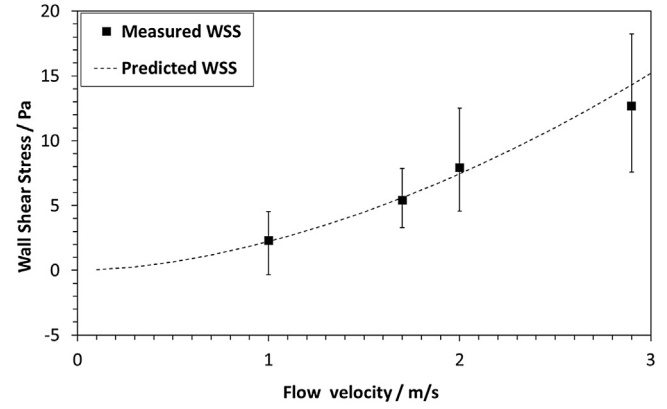

Fig. 7. Comparison of measured WSS values with Blasius calculations for pipe flow (10.2 cm ID).

For pipe flow, the Blasius friction factor for a smooth pipe wall was used [33]:

$$C_f = 0.079Re^{-1/4} \quad (4)$$

Since smooth walls were used in the present research, the measured WSS from experiments was compared to the calculated values for both channel and pipe flow. For channel flow there is a reasonably good agreement with the Patel correlation over a wide range of flow velocities (Fig. 6). The measurements from pipe flow are also consistent with the calculated values using the Blasius correlation (Fig. 7). The error bars in the graphs represent the maximum and minimum values of the WSS measurements. This agreement demonstrates that the WSS probe had been properly calibrated and was ready for application in two-phase flow conditions.

3.2. Wall shear stress measurements in gas-liquid two-phase flow

WSS in multiphase flow exhibits much more complicated behavior compared to single-phase flow, particularly due to the changes of the liquid phase distribution and velocity over time and in space. Since there are no well-established WSS correlations for multiphase flow, direct WSS measurements were seen as a means for contributing to a better understanding.

3.2.1. Wall shear stress measurements in slug flow

Slug flow is considered to be one of the most turbulent multiphase flow patterns [10]. Horizontal slug flow features a repetitive passage of slug units. A slug unit consists of a liquid slug body followed by a stratified zone. With high turbulence and gas/liquid mixing, the overall slug body moves at a mixture velocity averaged over the cross-section of the pipe, $V_m = V_{sl} + V_{sg}$. In the stratified zone, a relatively slow liquid film is moving at the bottom, with faster moving gas above it. Due to the inhomogeneous distribution of phases, the WSS values should be expected to be different around the pipe circumference.

Fig. 8(A) shows the data from a test at $V_{sl} = 2.0$ m/s and $V_{sg} = 2.1$ m/s with the WSS probe flush mounted at the bottom of the pipe. The evolution of WSS corresponds to the full measurement sequence for two-phase flow described earlier. Fig. 8(B) shows an expanded section of the WSS data taken at the bottom of the pipe for the fully developed slug flow, covering the time period between the dotted lines in Fig. 8(A). The expanded graph shows a series of distinct WSS peaks, which are presumably corresponding to the passages of slugs.

Fig. 9 shows a typical WSS measurement at the top of the pipe, which presents a different pattern, compared to that at the pipe bottom. The WSS peaks are more pronounced than those seen at the bottom, with much smaller base WSS values. The video data confirmed that the WSS peaks from both pipe bottom and top coincided with liquid slug body passages. Three peaks from both Figs. 8 (B) and 9 (B) are labeled with time stamps, which will be discussed in the next section. A number of WSS measurements were taken at the side wall of the pipe, which showed a similar pattern as that seen for the top and are therefore not shown here.

The different patterns of the WSS data seen for pipe bottom and top can be easily explained by the characteristics of horizontal slug flow. When the WSS probe was at the bottom, it was constantly immersed in a moving liquid phase, either in the form of a stratified film or a liquid slug body. As shown in Fig. 8(B), the base WSS value of about 15 Pa was due to the movement of the stratified film between the slugs, which caused peak WSS up to 29 Pa. On the other hand, when the WSS probe was at the top, there was a measurable WSS only when the liquid slug body was bridging the entire pipe cross section as it passed over the probe. Without the liquid slug, the gas phase exerted an unmeasurable WSS on the probe, due to its low density as compared to the liquid phase. This is evident by the WSS data shown in Fig. 9(B) where the measured WSS was almost zero between peaks, when no liquid slug body was present.

It was generally found that an increasing mixture velocity leads to an increasing WSS value at each of the probe locations. The maximum WSS values measured at the bottom, top and side of the pipe for each condition are tabulated in Appendix A. The maximum WSS value was determined by averaging the largest 20 values for each flow condition, in order to get a more representative value that can be used for modeling. To demonstrate this increase in WSS with increasing mixture velocity, Fig. 10 shows the maximum WSS value measured at the bottom of the pipe for each condition, overlain with the corresponding two-phase flow pattern map. It should be noted that in some of the test conditions stratified flow was predicted by the flow pattern map, while it was actually slug flow as confirmed by the video data. This is probably due to these conditions being close to the transition line between stratified flow and slug flow, and the inherent inaccuracy of the model used.

To interpret the measured maximum WSS in the slug body, stresses are compared with calculated values. Although there is no correlation for maximum WSS in slug flow, the mean WSS in the slug body (τ_s) has been calculated by using an equation similar to that for single-phase flow [34], as given by:

$$\tau_s = \frac{1}{2}\rho_s C_{f,s} V_s^2 \quad (5)$$

where ρ_s is the average fluid density of the slug body, $C_{f,s}$ is the Fanning friction factor of the slug body and V_s is the slug body velocity. The mixture velocity (V_m) is typically used as the slug body veloc-

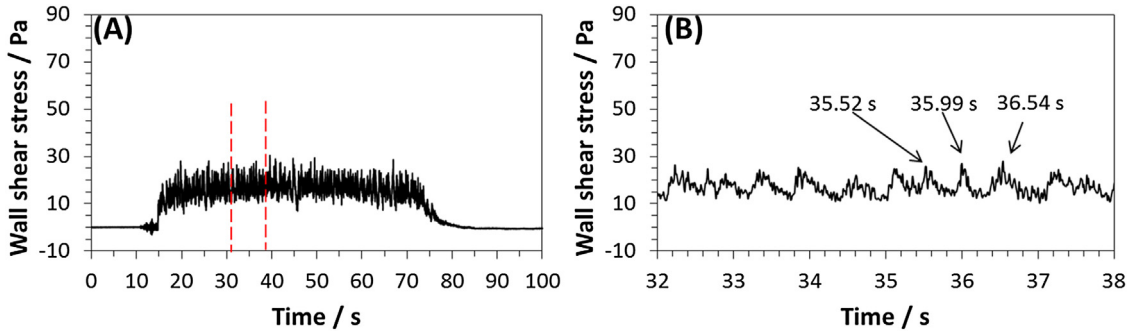

Fig. 8. Wall shear stress measurement at the bottom of the 10.2 cm pipe for V_{sl} = 2.0 m/s, V_{sg} = 2.1 m/s: (A) the full recording sequence; (B) data between the 32 and 38 s (fully developed flow).

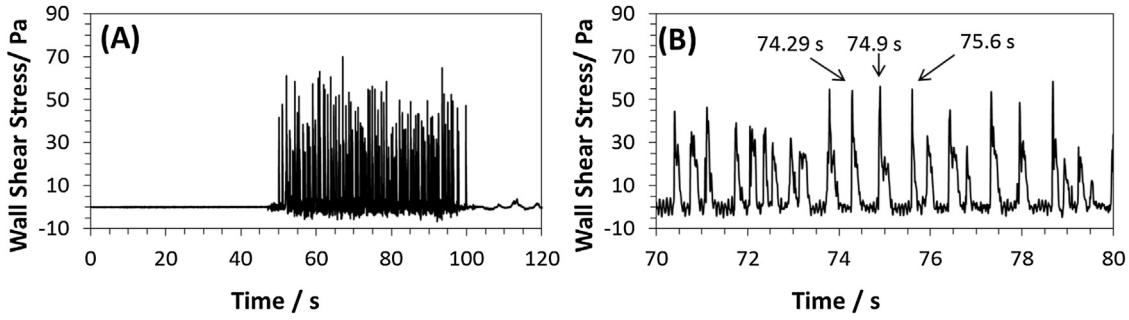

Fig. 9. Wall shear stress measurement at the top of the 10.2 cm pipe loop for V_{sl} = 2.0 m/s, V_{sg} = 2.6 m/s: (A) the full recording sequence; (B) data between 70 and 80 s.

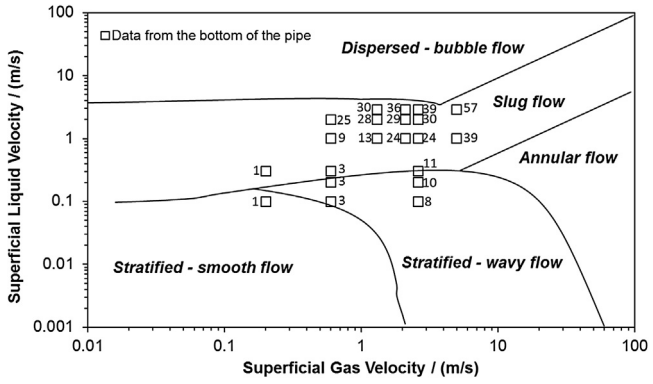

Fig. 10. τ_{max} (Pa) shown next to markers for slug flow measured at the bottom of the pipe overlain with the flow pattern map, at 1 bar, 25 °C, CO_2-water, and in the 10.2 cm loop.

ity in Eq. (5) to calculate the mean WSS, but the maximum local velocity is needed in order to calculate the maximum WSS. This local flow velocity is expected to be higher at the top of the pipe and lower at the bottom. To calculate the friction factor in Eq. (5), the Blasius-type correlation for smooth pipes was used:

$$C_{f,s} = 0.079 Re_s^{-1/4} \tag{6}$$

where the Reynolds number of the slug body (Re_s) using the pipe diameter (D) was written as:

$$Re_s = \frac{\rho_s D V_s}{\mu_s} \tag{7}$$

The average slug body density (ρ_s) and viscosity (μ_s) were calculated as:

$$\rho_s = \rho_L H_{ls} + \rho_G (1 - H_{ls}) \tag{8}$$

$$\mu_s = \mu_L H_{ls} + \mu_G (1 - H_{ls}) \tag{9}$$

where ρ_L and μ_L are the liquid density and viscosity, ρ_G and μ_G are the gas density and viscosity, and H_{ls} is the slug liquid holdup. A correlation for horizontal flow by Gregory et al. [35] was used to calculate the slug liquid holdup:

$$H_{ls} = \frac{1}{1 + \left(\frac{V_m}{8.66}\right)^{1.39}} \tag{10}$$

By using Eq. (5) through Eq. (10), the slug WSS can be calculated using the average slug body density and viscosity and a defined slug body velocity, as given by:

$$\tau_s = 0.0395 \cdot D^{-0.25} \rho_s^{0.75} \mu_s^{0.25} V_s^{1.75} \tag{11}$$

The mean WSS of the slug body is compared with the measured maximum WSS for each flow condition in Fig. 11. Generally, the measured maximum WSS values for all probe locations are higher than the calculated values when using the mixture velocity. This finding is important as many slug flow models only calculate the mean WSS of the slug body by using the mixture velocity, which can underestimate the maximum WSS by a large margin (a factor of 2–4). This finding also indicates that the highest WSS value occurred when the liquid slug passed the probe with a local velocity being higher than the mixture velocity. In addition, it was found that at the same flow condition, the maximum WSS at the top of the pipe was higher than that measured at the bottom of the pipe, while the maximum WSS measured at the sidewall was an intermediate value. It was assumed that the difference among the maximum WSS values at these three probe locations was due to the variation of the local liquid flow velocity in the slug body. In other words, the top part of the slug body had a higher maximum flow velocity than the bottom part of the slug body.

To better predict the maximum WSS, the maximum local velocity in the slug body is required. The in situ local velocity of the liquid in the slug body was determined by using the video data, as illustrated in Fig. 12. Two images of a liquid slug with a small time separation (Δt) of 0.003 s were compared. To determine actual liq-

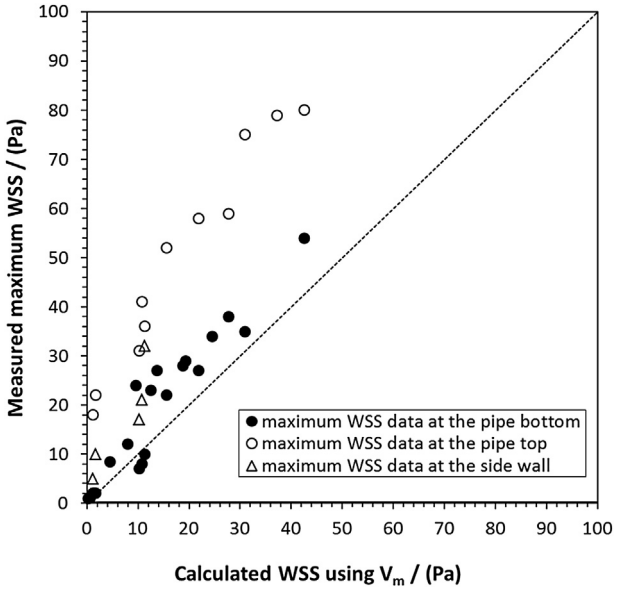

Fig. 11. Comparison between measured maximum WSS values and calculated mean slug WSS values from Eq. (11) by using mixture velocity (V_m), for 10.2 cm pipe loop.

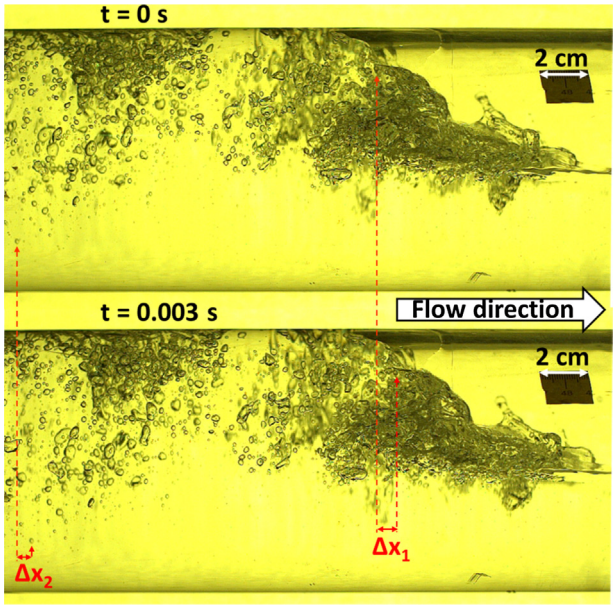

Fig. 12. Illustration of calculating the in situ liquid velocities in a slug body. Time difference between frames $\Delta t = 0.003$ s, $V_{sl} = 1.0$ m/s, $V_{sg} = 0.6$ m/s.

uid velocities, small gas bubbles, entrained by the liquid, were used as tracers to determine liquid velocities. For example, using Fig. 12, the in situ liquid velocity at the pipe top near the slug front was calculated as $\Delta x_1/\Delta t$. For lower quality images, the slug nose interface near the top was used as a tracer to estimate the liquid velocity. It should be noted that this interfacial velocity, or slug translational velocity, is not an actual liquid velocity. Because of the scooping up of the liquid from the stratified film into the slug body, the translational velocity is higher than the mixture velocity. Nevertheless, the translational velocity was deemed the maximum possible local velocity in the slug body [34]. Similarly, by tracking the horizontal movement of a small gas bubble in the slug body near the pipe bottom (Δx_2), the local liquid velocity at the pipe bottom was calculated as $\Delta x_2/\Delta t$. The horizontal movement was measured by using the 2-cm scale reference as shown in the images. Images of

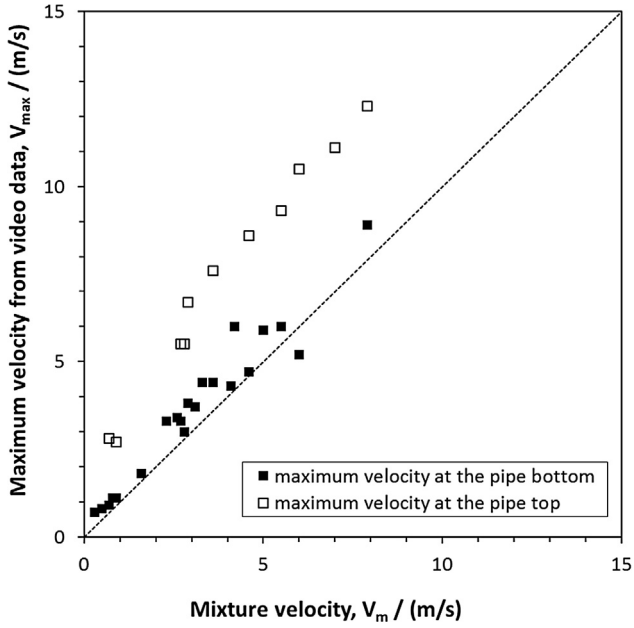

Fig. 13. Comparison between maximum local liquid velocity (V_{max}) in the slug body calculated from the video data and the mixture velocity (V_m) at each flow condition, for 10.2 cm pipe loop.

multiple slugs were analyzed for each flow condition and the maximum local velocities (V_{max}) at the top and bottom of the pipe were obtained (tabulated in Appendix B), which are compared with the mixture velocity in Fig. 13.

The comparison in Fig. 13 shows that the measured maximum liquid velocity at the bottom of the pipe is similar or slightly higher than the mixture velocity (within approximately 10%) while the maximum velocity at the top is significantly higher than the mixture velocity. As the cross-sectional average velocity in the slug body must be equal to the mixture velocity, this implies that sections of the fluid in the slug must be moving slower than the mixture velocity. Unfortunately, it was impossible to obtain the complete velocity profile from the existing video data due to the difficulties of tracking small individual gas bubbles.

Using the local maximum flow velocities (V_{max}) instead of the mixture velocities (V_m) for the slug body velocity (V_s), the maximum WSS was calculated using Eq. (11) and compared to the measured maximum WSS value (as shown in Fig. 14). The agreement between them demonstrates that the local WSS along the pipe periphery in the slug body can be calculated with a reasonable accuracy from Eq. (11) by using the true local flow velocity.

The WSS measurements in slug flow indicated that the flow velocity profile in the liquid slug body was highly non-uniform. The highest WSS occurred on the top of the pipe when the slug front passed with the maximum in situ flow velocity. The maximum WSS value was about 2–4 times higher than the calculated mean WSS value from empirical correlations when using the mixture velocity; this may serve as a guideline for operations involving slug flow and for slug flow modeling with applications to other areas, such as removal of corrosion inhibitor films and corrosion product layers.

3.2.2. Assessment of the location with the highest wall shear stress in a liquid slug body

In order to investigate the relationship between WSS measurements and flow patterns, a synchronized high speed camera was used in tandem with the WSS probe. This was done to assess which part of the liquid slug body would generate the highest WSS. Fig. 15 shows flow visualization frames of passing slug bodies corresponding to the WSS peak values that occur at 35.52 s, 35.99 s

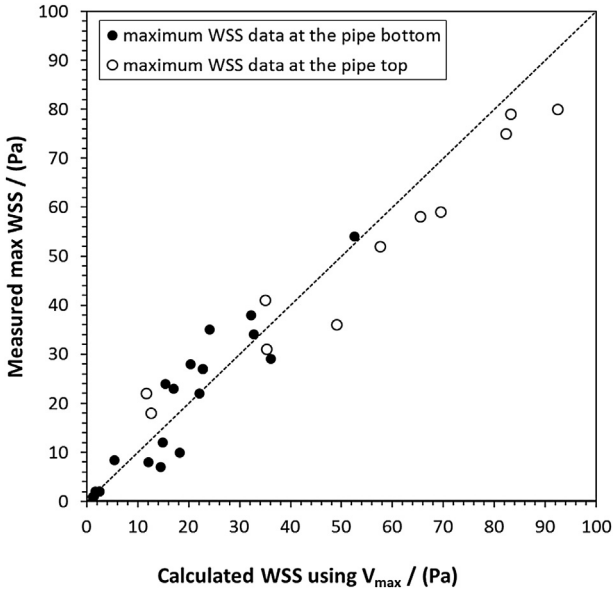

Fig. 14. Comparison between measured maximum WSS values and calculated maximum slug WSS values from Eq. (11) by using V_{max} from the video data, for 10.2 cm pipe loop.

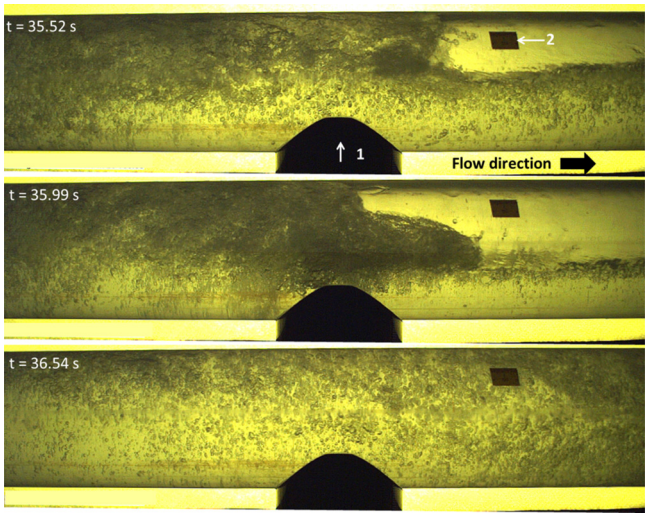

Fig. 15. Video frames of slug passages corresponding exactly to the three WSS measurement peaks marked in Fig. 8(B), V_{sl} = 2.0 m/s, V_{sg} = 2.1 m/s: 1. the WSS probe is at the pipe bottom; 2. a scale tape of 2 cm long.

and 36.54 s as marked in Fig. 8(B), respectively. In the images the WSS probe was masked by the black opaque probe holder and was flush mounted on the bottom pipe wall (at location "1" in Fig. 15). A 2 cm tape was attached to the front pipe wall as a length scale reference (marked as "2" in Fig. 15). In this specific flow condition, for the peaks at 35.52 s and 35.99 s, the highest bottom WSS value was recorded at exactly the same time when the slug front passed the WSS probe. However, for the peak at 36.54 s, the highest WSS was measured in the middle of the slug body. Considering all flow conditions documented by direct WSS measurements and high speed video recordings, no clear correlation was observed between the maximum WSS and a specific location in the slug body when the probe was at the bottom of the pipe. This can be explained by the difference between individual slugs formed in the 10.2 cm flow loop, having different flow characteristics at the bottom of the pipe.

When the probe was set at the top of the pipe, a clear correlation between the highest WSS and the passage of the slug front

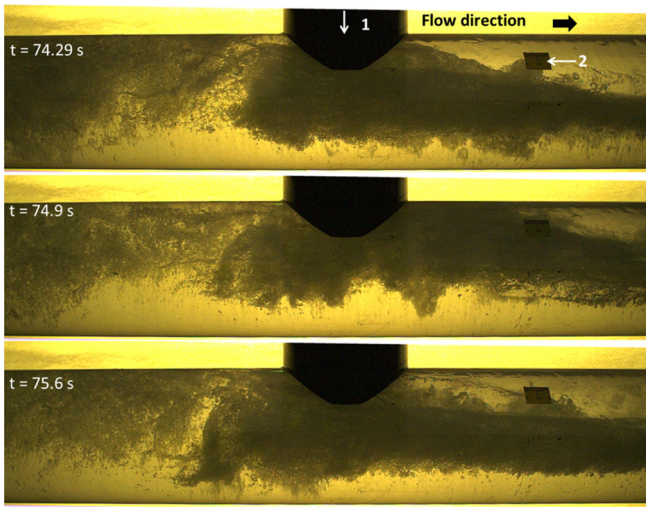

Fig. 16. Video frames of slug passages corresponding exactly to the three WSS measurement peaks marked in Fig. 9(B), V_{sl} = 2.0 m/s, V_{sg} = 2.6 m/s: 1. the WSS probe is at the pipe top; 2. a scale tape of 2 cm long.

was observed. Fig. 16 shows flow image frames corresponding to the three consecutive WSS peaks marked in Fig. 9(B). In this condition, the WSS peak values were always recorded at a time shortly after the slug fronts passed the WSS probe. This observation was repeatable and consistent for all slugs.

3.2.3. *Determination of slug frequency*

While not the main focus of this research, the slug frequency (slugs/second) was determined from two sources: from analyzing the high speed video recordings and the WSS data. From the video data, the slug frequency was obtained by visually counting the number of slugs per unit of time. From the WSS data taken at the top of the pipe, the slug frequency was determined by counting the WSS peaks per unit of time. For example, in Fig. 9(B), there are approximately 22 peaks within a 10 s period, which results in a slug frequency of 2.2 Hz. The measured slug frequencies are plotted in Fig. 17. Both methods should and did give almost the same results. The slug frequency increases with increasing superficial liquid velocity, and slightly decreases with increasing superficial gas velocity. The measured slug frequencies were compared with the data of Heywood and Richardson at similar flow conditions in a 42 mm ID pipe [36], as shown in Fig. 17. The results are coherent for these two sets of data even they were obtained in different pipe diameter systems. Existing literature reports that a minimum slug frequency can be determined as a function of V_{sg} for a given V_{sl} [36–38]. Gregory and Scott reported slug frequency data with a V_{sl} up to 1.3 m/s, and found the minima occurred at a slug translational velocity of approximate 6 m/s for each V_{sl} [37]. Woods et al. [38] found the minimum slug frequency to be at V_{sg} = 4 m/s in a 9.5 cm ID pipe for data with V_{sl} up to 1.2 m/s. In the present study, no clear minimum was observed, which may be due to the narrow superficial gas velocity range (up to 5 m/s).

The measured slug frequencies were also compared with several published empirical correlations as given in Table 3. The statistics related to the differences between the measured values and those predicted by the correlations are listed in Table 4. As it turns out, none of the predictions was satisfactory. The slug frequencies predicted by all correlations were significantly lower than the measured values. The results suggest that empirical correlations derived from a limited number of data in a specific test setup may not be reliable when applying them to systems where flow conditions (e.g., velocities, pipe diameters) are outside the original data set range. In addition, all existing empirical correlations may suffer

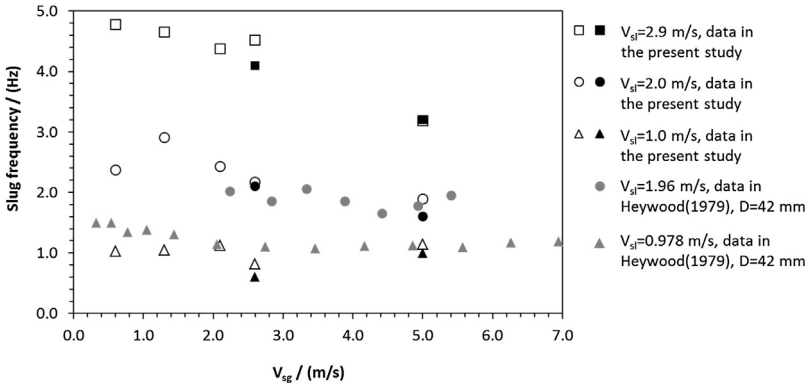

Fig. 17. Comparison of measured slug frequencies by different methods (video data: hollow markers; WSS data: solid black markers) with the data of Heywood and Richardson [36] (solid gray markers).

Table 3
Selected empirical correlations for slug frequency determination.

Heywood and Richardson [36] (1979)	$f_s = 0.0434\left[\frac{V_{sl}}{V_m}\left(\frac{2.02}{D}+\frac{V_m^2}{gD}\right)\right]^{1.02}$	(12)
Gregory and Scott [37] (1969)	$f_s = 0.0226\left[\frac{V_{sl}}{gD}\left(\frac{19.75}{V_m}+V_m\right)\right]^{1.2}$	(13)
Zabaras [40] (2000)	$f_s = 0.0226\left(\frac{V_{sl}}{gD}\right)^{1.2}\left[\frac{212.6}{V_m}+V_m\right]^{1.2}\left[0.836+2.75sin^{0.25}(\alpha)\right]$	(14)

Where f_s is the slug frequency (Hz), V_{sl} is the superficial liquid velocity, V_m is the mixture velocity, D is pipe diameter, g is gravitational acceleration and α is pipe inclination angle. It should be noted that the Heywood correlation [36] (1979) and the Gregory correlation [37] (1969) are given in SI units, while the Zabaras correlation [40] (2000) is written in English units with f_s in Hz, V_m and V_{sl} in ft/s, D in ft, α in degree and g in ft/s^2.

Table 4
Error statistics for slug frequency: (predicted − measured)/measured, for the data produced by using different empirical correlations.

Correlations	Heywood et al. [36]	Gregory et al. [37]	Zabaras [40]
Average error (%)	−59.3	−64.9	−70.7
Standard deviation (%)	12.0	9.2	7.7
Average absolute error (%)	59.3	64.9	70.7
Standard deviation of absolute error (%)	12.0	9.2	7.7

Table 5
WSS data measured for annular-mist flow at the bottom and the side wall of the 15.2 cm pipe.

Probe location	V_{sl}/(m/s)	V_{sg}/(m/s)	V_m/(m/s)	Mean WSS/(Pa)	Max WSS /(Pa)
bottom	0.02	42.2	42.22	8	14
bottom	0.1	42.2	42.30	13	19
bottom	0.2	42.2	42.40	25	32
side	0.02	42.2	42.22	0.5	4
side	0.1	42.2	42.30	2	9
side	0.2	42.2	42.40	3	9

to some degree from laboratory loop artefacts as the slug frequency in many laboratory facilities may be influenced by factors such as the inlet geometry, upstream details (e.g., presence of a gas buffer) and the length of the loop. Mechanistic approaches such as that given by, for example, the Taitel and Dukler model [39] are therefore recommended for accurate slug frequency predictions, even if these are much more complicated to implement [40].

3.2.4. Wall shear stress measurements in stratified flow and annular-mist flow

A limited number of WSS measurements were taken for stratified flow and annular-mist horizontal flow. For stratified flow, the liquid phase flows at the bottom of the pipe while the gas phase flows at the top. As the liquid and gas velocities are relatively low in this flow pattern, a low WSS is expected. The WSS values measured for stratified flow in the 10.2 cm loop were only up to 3 Pa at the tested flow conditions.

For annular-mist flow, a liquid film travels around the inner pipe periphery while the gas phase with high velocity flows in the core. Generally, part of the liquid will be entrained and travel as droplets/mist with the gas phase. The WSS was measured at the bottom and the side of the 15.2 cm ID pipe system (Fig. 5), with the values given in Table 5. There was no measurable WSS at the top of the pipe at the tested conditions. The WSS values for the bottom and the side increased with increasing liquid superficial velocity. The WSS at the side wall was smaller than that at the bottom of the pipe. This was mainly due to the much smaller thickness of the moving liquid film, and presumably a smaller liquid velocity, for the side as compared to the bottom of the pipe.

4. Discussion

In the present research project, two-phase pipe flow patterns such as slug flow, stratified flow and annular-mist flow were investigated, and the highest WSS recorded was of the order of 100 Pa. These high values were recorded for slug flow at the top of the pipe when each slug front passed. Measured WSS values were in agreement with empirical WSS correlations when using the correct local velocities in the two-phase flow field. This suggests that proper resolution of the flow field, obtained either from computational fluid dynamics or by experimentation, would allow for better evaluation of WSS.

In laboratory environments, inhibitors are often subjected to high flow velocity tests with calculated WSS of the order of 10^3 Pa [19,41] to assess their performance in "extreme" flow conditions. In the present research conducted in single-phase channel flow, the measured WSS reached the same magnitude of 10^3 Pa when the liquid velocity was extremely high (17 m/s), but for the measured two-phase slug flow with the mixture velocity up to 7.9 m/s, the highest WSS values were one order of magnitude lower. When using Eq. (11) as a reference to calculate the WSS of slug flow under hypothetical flow conditions, it was found that the maximum value would not exceed 1000 Pa even with mixture velocities up to 30 m/s and gas densities up to 100 kg/m^3 (in a 10.2 cm ID

pipe). This suggests that the maximum WSS in realistic multiphase pipe flow under most extreme conditions would be of the order of 10^3 Pa.

Recalling the fact that the stresses required to remove inhibitor films and/or protective corrosion product layers are at least 10^6 Pa [8,15,20,24], there is a large gap between the required stresses to remove these films/layers and flow WSS measured or expected in practical applications. It may therefore be concluded that the high values of WSS found in multiphase flow cannot lead to purely mechanical removal of inhibitor films and protective corrosion product layers.

Although the floating element probe was used to successfully measure the WSS in the multiphase flow, some possible shortcomings in the present research program have been identified and are discussed below. The spatial and temporal resolutions of the WSS probe do not allow to measure very short-lived WSS (fluctuations) occurring over very small length scales.

The floating element on the WSS probe has a diameter of 6 mm, which still can be much larger than the length scale of some turbulent eddies. The smallest hydrodynamic scale in turbulent flow can be estimated by the Kolmogorov length scale (η), which is approximately of the order of 10–100 μm in laboratory environments such as the one used here [42,43]. Therefore, to accurately measure local WSS fluctuations due to the smallest of turbulent eddies, a floating element with spatial dimensions of the order of 10–100 μm may be necessary. The time scales associated with the smallest of eddies are of the order of ms, or even less, putting an additional requirement on the temporal resolution of the measurements. On the other hand, the energy levels associated with the smallest eddies are also very low and it is not expected that they can contribute to a significant increase of the time/space averaged WSS, such as the one measured here.

Using the highest recording rate of 1000 Hz, the WSS probe provided reasonable measurements when it comes to the large time scale transients found in multiphase flows, such as, for example, during slugging. For instance, the slug frequency was only a few hertz, and any WSS fluctuations due to the passage of slugs would have been accurately recorded by the floating element probe.

While a number of different multiphase flow patterns were investigated in the present work, it is believed that some specific flow conditions found in the field, involving a discrete phase, were not covered by our testing. A good example is liquid droplet impingement found in annular-mist flow which may lead to much larger fluctuations of the WSS magnitude than recorded in the present study. Annular-mist flow with entrained liquid droplets, traveling at the gas velocity, can lead to high energy wall impacts particularly at locations of disturbed flow, such as bends, valves, tees, weld beads, etc. Very high local WSS and normal stresses could be found at impact locations [44], particularly when there is little "cushioning" by an existing liquid film. Laboratory tests have shown entrained droplets having sizes of the order of 100 μm [45], which would produce very short lived, high energy fluctuations at impact time. Therefore, a WSS probe would be required to have both high temporal and spatial resolutions in order to capture this behavior. This is an area that needs to be covered by future research.

5. Conclusions

Several conclusions can be drawn based on the present research results:

1) The floating element method was successful in directly measuring wall shear stresses in multiphase flow, which provides valuable data for mechanistic modeling.
2) The highest wall shear stress found in horizontal slug flow occurred on the top section of the pipe when the slug front passed. The higher wall shear stress at the top as compared to the bottom of the pipe was because of the higher local in situ liquid flow velocity. The maximum wall shear stress value was about 2–4 times higher than the mean wall shear stress in the slug body calculated using the mixture velocity, which can serve as a guideline for improving slug flow modeling. When the correct local velocity is used, the calculations of the wall shear stress were in good agreement with the measured values.
3) In multiphase flow, studied here at ambient conditions, the maximum measured wall shear stress was of the order of 10^2 Pa, obtained in slug flow. Using a model it was estimated that the highest practical wall shear stress that could be expected in the field is of the order of 10^3 Pa.
4) This suggests that purely mechanical removal of inhibitor films or corrosion product layers solely by wall shear stress, typically seen in multiphase flow pipelines, is very unlikely. As failures of these protective films/layers in multiphase flow are observed in laboratory and field studies, other factors associated with multiphase flow must be considered.

Acknowledgements

The research was financially sponsored from the Corrosion Center Joint Industry Project in the Institute for Corrosion and Multiphase Technology at Ohio University. Part of the data was presented in the paper no. 5922 at the NACE International CORROSION 2015 Conference (held in Dallas, Texas, USA, March 2015).

Appendix A.

Wall shear stress measurements for slug flow in the 10.2 cm pipe loop.

Probe location	V_{sl} /(m/s)	V_{sg} /(m/s)	V_m /(m/s)	Max WSS /(Pa)
Bottom	0.1	0.2	0.3	1
Bottom	0.1	0.6	0.7	2
Bottom	0.1	2.6	2.7	7
Bottom	0.2	0.6	0.8	2
Bottom	0.2	2.6	2.8	8
Bottom	0.3	0.2	0.5	1
Bottom	0.3	0.6	0.9	2
Bottom	0.3	2.6	2.9	10
Bottom	1.0	0.6	1.6	9
Bottom	1.0	1.3	2.3	12
Bottom	1.0	2.1	3.1	23
Bottom	1.0	2.6	3.6	22
Bottom	1.0	5.0	6.0	35
Bottom	2.0	0.6	2.6	24
Bottom	2.0	1.3	3.3	27
Bottom	2.0	2.1	4.1	28
Bottom	2.0	2.6	4.6	27
Bottom	2.9	1.3	4.2	29
Bottom	2.9	2.1	5.0	34
Bottom	2.9	2.6	5.5	38
Bottom	2.9	5.0	7.9	54
Top	0.1	0.6	0.7	18
Top	0.1	2.6	2.7	31
Top	0.2	2.6	2.8	41
Top	0.3	0.6	0.9	22
Top	0.3	2.6	2.9	36
Top	1.0	2.6	3.6	52
Top	1.0	5.0	6.0	75
Top	2.0	2.6	4.6	58
Top	2.0	5.0	7.0	79
Top	2.9	2.6	5.5	59
Top	2.9	5.0	7.9	80
Side	0.1	0.6	0.7	5
Side	0.1	2.6	2.7	17
Side	0.2	2.6	2.8	21
Side	0.3	0.6	0.9	10
Side	0.3	2.6	2.9	32

Appendix B.

Maximum local liquid velocity (V_{max}) calculated from the video data in the slug body, for 10.2 cm pipe loop.

Location	V_{sl}/(m/s)	V_{sg}/(m/s)	V_m/(m/s)	V_{max}/(m/s)
Bottom	0.1	0.2	0.3	0.7
Bottom	0.1	0.6	0.7	0.9
Bottom	0.1	2.6	2.7	3.3
Bottom	0.2	0.6	0.8	1.1
Bottom	0.2	2.6	2.8	3.0
Bottom	0.3	0.2	0.5	0.8
Bottom	0.3	0.6	0.9	1.1
Bottom	0.3	2.6	2.9	3.8
Bottom	1.0	0.6	1.6	1.8
Bottom	1.0	1.3	2.3	3.3
Bottom	1.0	2.1	3.1	3.7
Bottom	1.0	2.6	3.6	4.4
Bottom	1.0	5.0	6.0	5.2
Bottom	2.0	0.6	2.6	3.4
Bottom	2.0	1.3	3.3	4.4
Bottom	2.0	2.1	4.1	4.3
Bottom	2.0	2.6	4.6	4.7
Bottom	2.9	1.3	4.2	6.0
Bottom	2.9	2.1	5.0	5.9
Bottom	2.9	2.6	5.5	6.0
Bottom	2.9	5.0	7.9	8.9
Top	0.1	0.6	0.7	2.8
Top	0.1	2.6	2.7	5.5
Top	0.2	2.6	2.8	5.5
Top	0.3	0.6	0.9	2.7
Top	0.3	2.6	2.9	6.7
Top	1.0	2.6	3.6	7.6
Top	1.0	5.0	6.0	10.5
Top	2.0	2.6	4.6	8.6
Top	2.0	5.0	7.0	11.1
Top	2.9	2.6	5.5	9.3
Top	2.9	5.0	7.9	12.3

References

[1] S. Nesic, W. Sun, Corrosion in acid gas solutions, in: J.A. Richardson, et al. (Eds.), Shreir's Corrosion, Elsevier, Amsterdam, The Netherlands, 2010, pp. 1270–1298.

[2] S. Nesic, Carbon dioxide corrosion of mild steel, in: R. Winston Revie (Ed.), Uhlig's Corrosion Handbook, 3rd edition, John Wiley & Sons, Inc., Hoboken, New Jersey, 2011, pp. 229–245.

[3] S. Ramachandran, B.-L. Tsai, M. Blanco, H. Chen, Y. Tang, W.A. Goddard III, Self-assembled monolayer mechanism for corrosion inhibition of iron by imidazolines, Langmuir 12 (1996) 6419–6428.

[4] J. Han, D. Young, H. Colijn, A. Tripathi, S. Nesic, Chemistry and structure of the passive film on mild steel in CO_2 corrosion environments, Ind. Eng. Chem. Res. 48 (2009) 6296–6302.

[5] J. Zhang, Z.L. Wang, Z.M. Wang, X. Han, Chemical analysis of the initial corrosion layer on pipeline steels in simulated CO_2-enhanced oil recovery brines, Corros. Sci. 65 (2012) 397–404.

[6] W. Li, B. Brown, D. Young, S. Nesic, Investigation of pseudo-passivation of mild steel in CO_2 corrosion, Corrosion 70 (2014) 294–302.

[7] H. Liu, T. Gu, G. Zhang, W. Wang, S. Dong, Y. Cheng, H. Liu, Corrosion inhibition of carbon steel in CO_2-containing oilfield produced water in the presence of iron-oxidizing bacteria and inhibitors, Corros. Sci. 105 (2016) 149–160.

[8] R.H. Hausler, G. Schmitt, Hydrodynamic and flow effects on corrosion inhibition, NACE International CORROSION/2004 conference, paper no. 04402.

[9] G.A. Zhang, N. Yu, L.Y. Yang, X.P. Guo, Galvanic corrosion behavior of deposit-covered and uncovered carbon steel, Corros. Sci. 86 (2014) 202–212.

[10] S. Nesic, Effects of multiphase flow on internal CO_2 corrosion of mild steel pipelines, Energy Fuels 26 (2012) 4098–4111.

[11] T. Hara, H. Asahi, Y. Suehiro, H. Kaneta, Effect of flow velocity on carbon dioxide corrosion behavior in oil and gas environments, Corrosion (2000) 860–866.

[12] V. Ruzic, M. Veidt, S. Nesic, Protective iron carbonate films –part 1: mechanical removal in single-phase aqueous flow, Corrosion 62 (2006) 419–432.

[13] G. Schmitt, M. Mueller, Critical wall shear stresses in CO_2 corrosion of carbon steel, NACE International CORROSION/99 conference, paper no. 44.

[14] B.F.M. Pots, E. Hendriksen, H. de Reus, H. Pit, S. Paterson, Field study of corrosion inhibition at very high flow velocity, NACE International CORROSION/2003 conference, paper no. 03321.

[15] K. Gao, F. Yu, X. Pang, G. Zhang, L. Qiao, W. Chu, M. Lu, Mechanical properties of CO_2 corrosion product scales and their relationship to corrosion rates, Corros. Sci. 50 (2008) 2796–2803.

[16] B. Poulson, Advances in understanding hydrodynamic effects on corrosion, Corros. Sci. 35 (1993) 655–665.

[17] S. Seal, K. Sapre, A. Kale, V. Desai, M. Gopal, P. Jepson, Effect of multiphase flow on corrosion of C-steel in presence of inhibitor: a surface morphological and chemical study, Corros. Sci. 42 (2000) 1623–1634.

[18] L. Zeng, G.A. Zhang, X.P. Guo, C.W. Chai, Inhibition effect of thioureidoimidazoline inhibitor for the flow accelerated corrosion of an elbow, Corros. Sci. 90 (2015) 202–215.

[19] E. Gulbrandsen, A. Grana, Testing of carbon dioxide corrosion inhibitor performance at high flow velocities in jet impingement geometry. Effects of mass transfer and flow forces, Corrosion 63 (2007) 1009–1020.

[20] Y. Yang, B. Brown, S. Nesic, M. Elena Gennaro, B. Molinas, Mechanical strength and removal of a protective iron carbonate layer formed on mild steel in CO_2 corrosion, NACE International CORROSION/2010 conference, paper no. 10383.

[21] J. Huang, B. Brown, S. Nesic, Localized corrosion of mild steel under silica deposits in inhibited aqueous CO_2 solutions, NACE International CORROSION/2013 conference, paper no. 2144.

[22] J.R. Shadley, S.A. Shirazi, E. Dayalan, E.F. Rybicki, Prediction of erosion-corrosion penetration rate in a carbon dioxide environment with sand, Corrosion 54 (1998) 972–978.

[23] R. Barker, A. Neville, X. Hu, S. Cushnaghan, Evaluating inhibitor performance in CO_2-saturated erosion-corrosion environments, Corrosion 71 (2015) 14–29.

[24] Y. Xiong, B. Brown, B. Kinsella, S. Nesic, A. Pailleret, Atomic force microscopy study of the adsorption of surfactant corrosion inhibitor films, Corrosion 70 (2014) 247–260.

[25] G. Schmitt, C. Bosch, P. Plagemann, K. Moeller, Local wall shear stress gradients in the slug flow regime—effects of hydrocarbon and corrosion inhibitor, NACE international CORROSION/2002 conference, paper no. 02244.

[26] V.E. Nakoryakov, O.N. Kashinsky, A.P. Burdukov, V.P. Odnoral, Local characteristics of upward gas-liquid flows, Int. J. Multiphase Flow 7 (1981) 63–81.

[27] H. Wang, T. Hong, J.Y. Cai, W.P. Jepson, C. Bosch, Enhanced mass transfer and wall shear stress in multiphase slug flow, NACE International CORROSION/2002 conference, paper no. 02501.

[28] T.K. Villiger, M. Morbidelli, M. Soos, Experimental determination of maximum effective hydrodynamic stress in multiphase flow using shear sensitive aggregates, AIChE J. 61 (2015) 1735–1744.

[29] J.W. Naughton, M. Sheplak, Modern development in shear-stress measurement, Prog. Aerosp. Sci. 38 (2002) 515–570.

[30] T.J. Hanratty, J.A. Campbell, Measurement of wall shear stress, in: R.J. Goldstein (Ed.), Fluid Mechanics Measurements, 2nd edition, Taylor & Francis, Washington, DC, 1996, pp. 575–649.

[31] V. Sheverev, V. Stepaniuk, Shear stress measurement apparatus, US patent no. US 8, 276, 463 B2, 2012.

[32] S. Nesic, S. Wang, J. Cai, Y. Xiao, Integrated CO_2 corrosion—multiphase flow model, NACE International CORROSION/2004 conference, paper no. 04626.

[33] V.C. Patel, M.R. Head, Some observations on skin friction and velocity profiles in fully developed pipe and channel flows, J. Fluid Mech. 38 (1969) 181–201.

[34] O. Shoham, Mechanistic Modeling of Gas-Liquid Two-Phase Flow in Pipes, Society of Petroleum Engineers, Richardson, Texas, 2006.

[35] G.A. Gregory, M.K. Nicholson, K. Aziz, Correlation of the liquid volume fraction in the slug for horizontal gas-liquid slug flow, Int. J. Multiphase Flow 4 (1978) 33–39.

[36] N.I. Heywood, J.F. Richardson, Slug flow of air-water mixtures in a horizontal pipe: determination of liquid holdup by γ-ray absorption, Chem. Eng. Sci. 34 (1979) 17–30.

[37] G.A. Gregory, D.S. Scott, Correlation of liquid slug velocity and frequency in horizontal concurrent gas-liquid slug flow, AIChE J. 15 (1969) 933–935.

[38] B.D. Woods, Z. Fan, T.J. Hanratty, Frequency and development of slugs in a horizontal pipe at large liquid flows, Int. J. Multiphase Flow 32 (2006) 902–925.

[39] Y. Taitel, A.E. Dukler, A model for slug frequency during gas-liquid flow in horizontal and near horizontal pipes, Int. J. Multiphase Flow 3 (1977) 585–596.

[40] G.J. Zabaras, Prediction of slug frequency for gas/liquid flows, SPE J. 5 (2000) 252–258.

[41] R. Barker, X. Hu, A. Neville, S. Cushnaghan, Assessment of preferential weld corrosion of carbon steel pipework in CO_2-saturated flow-induced corrosion environments, Corrosion 69 (2013) 1132–1143.

[42] G.A. Voth, A. La Porta, A.M. Crawford, J. Alexander, E. Bodenschatz, Measurement of particle accelerations in fully developed turbulence, J. Fluid Mech. 469 (2002) 121–260.

[43] H. Xu, E. Bodenschatz, Motion of inertial particles with size larger than Kolmogorov scale in turbulent flows, Physica D 237 (2008) 2095–2100.

[44] J.H. Gerretsen, A. Visser, Inhibitor performance under liquid droplet impingement conditions in CO_2-containing environment, Corros. Sci. 34 (1993) 1299–1310.

[45] A. Al-Sarkhi, T.J. Hanratty, Effect of pipe diameter on the drop size in a horizontal annular gas-liquid flow, Int. J. Multiphase Flow 28 (2002) 1617–1629.